

## Research



**Cite this article:** Fan X, Swartz S, Breuer K. 2022 Power requirements for bat-inspired flapping flight with heavy, highly articulated and cambered wings. *J. R. Soc. Interface* **19**: 20220315.  
<https://doi.org/10.1098/rsif.2022.0315>

Received: 22 April 2022  
Accepted: 25 August 2022

**Subject Category:**  
Life Sciences—Physics interface

**Subject Areas:**  
biomechanics

**Keywords:**  
power expenditure, flapping wing, bat flight

**Author for correspondence:**  
Xiaozhou Fan  
e-mail: xzfan@brown.edu

Electronic supplementary material is available online at <https://doi.org/10.6084/m9.figshare.c.6181102>.

# Power requirements for bat-inspired flapping flight with heavy, highly articulated and cambered wings

Xiaozhou Fan<sup>1</sup>, Sharon Swartz<sup>1,2</sup> and Kenneth Breuer<sup>1,2</sup>

<sup>1</sup>Center for Fluid Mechanics, School of Engineering, Brown University, and <sup>2</sup>Department of Ecology, Evolution, and Organismal Biology, Aeromechanics & Evolutionary Morphology Lab, Brown University, Providence, RI, USA

XF, 0000-0002-6841-6606; SS, 0000-0001-5762-7435; KB, 0000-0002-5122-2231

Bats fly with highly articulated and heavy wings. To understand their power requirements, we develop a three-dimensional reduced-order model, and apply it to flights of *Cynopterus brachyotis*, the lesser dog-faced fruit bat. Using previously measured wing kinematics, the model computes aerodynamic forces using blade element momentum theory, and incorporates inertial forces of the flapping wing using the measured mass distribution of the membrane wing and body. The two are combined into a Lagrangian equation of motion, and we performed Monte Carlo simulations to address uncertainties in measurement errors and modelling assumptions. We find that the camber of the armwing decreases with flight speed whereas the handwing camber is more independent of speed. Wing camber disproportionately impacts energetics, mainly during the downstroke, and increases the power requirement from 8% to 22% over flight speed  $U = 3.2\text{--}7.4\text{ m s}^{-1}$ . We separate total power into aerodynamic and inertial components, and aerodynamic power into parasitic, profile and induced power, and find strong agreement with previous theoretical and experimental studies. We find that inertia of wings help to balance aerodynamic forces, alleviating the muscle power required for weight support and thrust generation. Furthermore, the model suggests aerodynamic forces assist in lifting the heavy wing during upstroke.

## 1. Introduction

The study of flapping flight energetics has grown steadily for nearly 50 years [1]. Using diverse methods, the aerodynamic and inertial power necessary to move through air has been studied in a broad range of flying animals, from small insects to larger bats and birds [2–11].

Pennycuik adapted blade element momentum theory (BEMT), rooted in helicopter aerodynamics [12], to analyse bird flight energetics, and argued for exclusion of inertial power—the work required to move wing mass—from these models, viewing wing kinetic energy as a source of useful work [9]. In this view, Pennycuik highlighted a key aspect of inertial power: a flapping bird can divert some inertial energy towards aerodynamic work during the downstroke [9]. Rayner [2,13,14] modelled the fluid wake behind slow-flying birds as vortex rings convected with the freestream; he used this approach to derive a widely used model for aerodynamic power. More recently, explicit links between flapping flight parameters (thrust ratios, reduced frequencies and stroke-plane angles) and the components of aerodynamic power (profile, parasitic and induced power) have been made using nonlinear regression models [15]. However, all theoretical models published to date need various empirical correction factors to accurately predict power expenditures (for example, an induced velocity correction factor [9,16–18] or a profile power coefficient [2,15]). Moreover, power predictions made using these models can be very sensitive to the values of these empirical constants. Broad application of these models may also be limited by typical assumptions concerning laminar

boundary profiles, which are used to estimate the zero-lift drag coefficients  $C_{D0}$ ; it is likely that these assumptions do not hold for animals with micro-structured wings, where a turbulent boundary layer may be present [19], and thus the assumed values of zero-lift drag coefficients have large deviation from the measured ones [20]. Particle image velocimetry (PIV) techniques have been employed to measure the wake velocity fields behind flying animals [21–24], and used to study flight energetics. However, viscous diffusion and wake deformation may play a significant role in measurement accuracy [21]. Vertical force is, in general, effectively estimated from wake reconstruction, but the much smaller thrust measurements are more challenging (exception for lift-based thrust [25]). Moreover, PIV experiments cannot measure the force and power related to wing inertia.

Physical models—using engineered robotic platform—can assess flight power as a complement to live animal experiments. A bat-inspired robotic wing was built that mimicked flapping and retraction/protraction of the lesser dog-faced fruit bat, *Cynopterus brachyotis*, and torques were directly measured from the motor for a range of wing kinematics and airspeeds [26,27]. Such models, however, often fail to capture the details of complex kinematics observed in flying animals, such as in the case of Bahlman's robotic wing [26,27], in which prominent twisting and folding motions of the wing during upstroke are not present [28,29].

Lastly, computational fluid dynamics (CFD) offers another approach for flight power estimation. Large eddy simulation tracks important flow structures, such as the leading edge vortex (LEV), in space and time, and predicts temporal evolution of power expenditure, an important refinement compared with cycle-averaged values. However, this approach requires very large computational resources, which renders parametric studies that might contribute to understanding power consumption difficult [11,28].

A 'Goldilocks' approach—one that captures good fidelity at reasonable computational cost—is the use of low-order modelling [10,29–31]. Norberg [32] employed this approach to create a fixed-wing model of flight in brown long-eared bats, *Plecotus auritus*, that included inertial effects, and concluded that the slow flapping flight is well modelled by quasi-steady assumptions. Parslew simulated power-optimal hovering, cruising, climbing and descending flight in pigeons, *Columba livia*, and found the most efficient kinematics differ for hovering versus forward flight [33].

To date, however, the potential of this reduced-order modelling has yet to be fully realized, especially for the highly articulated flyers such as bats or birds. Key shortcomings have included a lack of detailed kinematics [34], which has led to failure to resolve nuanced yet important wing kinematic features. Wing camber [35,36], for example, which has disproportionate aerodynamic effects [29], is all but absent in power estimation among reduced-order modelling studies published to date. In addition, they fail to implement unconstrained, free flight for flyers with relatively heavy wings (bats and some birds), which results in incomplete energetic models [2,9]. Moreover, changes in inertial forces due to wing flexion are not present [32], which prove to be important in some animals [37].

To address these shortcomings, we report here on a novel low-order model which can be used to study the power expenditure of flapping animals. Although it could be applied quite generally, in this manuscript, we consider the

flight of *Cynopterus brachyotis*, a frugivorous bat of moderate size, over a range of speeds. The model is an extension of previous work in our group (Fan & Breuer [29]), in which we demonstrated the accuracy and generality of the approach using kinematics derived from the flight of *Cynopterus brachyotis* at a single flight speed of  $4.8 \text{ m s}^{-1}$ . Briefly, the model uses prescribed kinematics, in this case based directly on detailed measurements of flying bats [34], allowing for the quantification of the role of wing camber on aerodynamics and power estimation. Coupled to a quasi-steady aerodynamic model, this approach uses a full, unconstrained inertial model to predict flight behaviour. The only empirical coefficients required are lift and drag functions, which relate angle of attack to lift and drag for each wing segment; the results are, moreover, robust to reasonable uncertainty with regard to this aerodynamic model. A key benefit of this approach is that it determines both inertial and aerodynamic power, and can further decompose aerodynamic power into its four fundamental components: induced, parasitic, profile and climbing power [17]. Unlike a robotic wing platform, the temporal force data output by the model do not suffer from parasitic forces associated with the experimental platform [26]. Furthermore, in this formulation, the thrust/drag can be directly computed, unlike the case for experiments, where the thrust/drag measurement is difficult [7]. This low-order modelling approach is cheap in computational time and resources. We assess the model's robustness by Monte Carlo error estimates, in which we use slightly perturbed input parameters to quantitatively bound the computed power uncertainties, and demonstrate the model's potential impact and effectiveness on cost of flight in *Cynopterus brachyotis* over a range of flight speeds.

The present manuscript extends our previous work [29] in several important aspects. Firstly, we focus here on the power requirements for flight, using the low-order modelling approach, to separate out contributions due to aerodynamic and inertial forces, as well as the energetic expenditure associated with wing camber. Secondly, we apply this novel approach to several flights over a range of flight speeds, rather than the single flight speed ( $4.8 \text{ m s}^{-1}$ ) in our previous work. The results are compared with other cost-of-flight estimates from a variety of other recent studies that employed different techniques (PIV, CFD and analytical modelling).

## 2. Methods

### 2.1. Kinematic data and low-order modelling

Flight kinematics are taken from previously reported measurements of the lesser dog-faced fruit bat, *Cynopterus brachyotis*, flying in a wind tunnel [34,37]. These animals are medium-sized fruit-eating, non-echolocating bats, weighing about 34 g. Whereas Fan & Breuer [29] analysed only one trial to demonstrate the use of the low-order quasi-steady computational model, here we use kinematic data from trials recorded at six flight speeds,  $U$ , ranging from  $3.2$  to  $7.4 \text{ m s}^{-1}$ , corresponding to chord ( $c$ ) Reynolds number,  $Re = U c / \nu$ , ranging from 10 500 to 24 500, where  $\nu$  is the kinematic viscosity of air. Strouhal numbers,  $St = f h_a / U$ , where  $f$  is the flapping frequency, and  $h_a$  is the vertical displacement of wing tip [38], ranged between 0.27 and 0.4—typical for animals in cruising flight [39]. The experimentally measured kinematics describe the motion of bat body (four markers) and the left wing (40 markers, figure 1a). Since

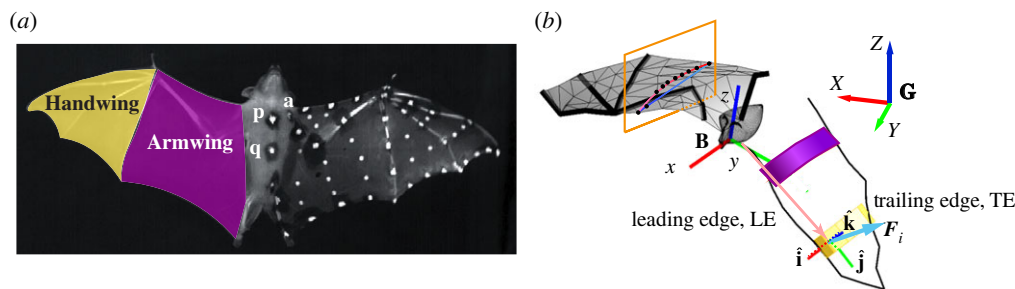


**Figure 1.** Marker patterns and establishment of coordinates. (a) ‘p’ (sternum), ‘q’ (lumbar) and ‘a’ (shoulder) markers construct the body-fixed coordinate system  $\mathbf{B}$ , in which the armwing (purple) and a handwing (gold) are analysed. (b) Global coordinate,  $\mathbf{G}$ , body-fixed coordinate,  $\mathbf{B}$ , and a segment in the armwing (purple) and handwing (gold), respectively. Each segment has its own local axis coordinate as demonstrated in the handwing segment. The aerodynamic force (light blue) imparted at the quarter-chord will result in a torque and a force at the shoulder, which is in the local wing segment plane spanned by  $\hat{i}$  and  $\hat{k}$ . The displacement vector (pink arrow) indicates the moment arm. For each wing segment at every instant, a cutting plane (orange box) intersects with the wing surface mesh (black points) and the intersection of the cutting plane and the wing surface mesh are fitted with a Fourier series to represent angle of attack (blue chord line) and camber (red curve, which ultimately translates to zero-lift angle of attack [40]).

all of the flights considered are straight, the right wing motion is assumed to be a mirror image of the left wing.

The calculation of flight power is made using the low-order model described in detail by Fan & Breuer [29]. For convenience, key elements of the computational approach are summarized here. Inertial forces are computed from the measured wing kinematics, and the known mass of bones, muscles, connective tissues and wing membrane [29,41]. Each wing and the torso are then represented by a point mass with a defined rotational moment of inertia.

To model the aerodynamic forces, the wing is segmented into  $N = 10$  discrete blade elements [42], and each blade element has 6 degrees of freedom (d.f.) ( $x_i, y_i, z_i, \phi_i, \psi_i, \theta_i$ ), defined in the body-fixed coordinate  $\mathbf{B}$  [29], where the subscript  $i$  runs from 1 to  $N$  to index the discrete wing segments,  $x_i, y_i, z_i$  are the quarter-chord location for  $i$ th segment, and  $\phi_i, \psi_i, \theta_i$  represent the orientation of the segment in Euler angles. Each blade element is modelled as a two-dimensional thin aerofoil with camber (figure 1b). Using the angle of attack,  $\alpha$ , and chord-normalized camber,  $z_{\max}/c$ , of each measured wing segment profile, lift and drag coefficients,  $C_l$  and  $C_d$ , respectively, are assigned using the empirical values of Usherwood [43]:

$$C_l = 1.6 \sin(2(\alpha - \alpha_0)) \quad (2.1)$$

and

$$C_d = 1.135 - 1.05 \cos(2(\alpha - \alpha_0)), \quad (2.2)$$

where  $\alpha_0$  is the zero-lift angle of attack, and is a function of camber,  $z_{\max}/c$  from thin aerofoil theory [40]. An iterative wake model [29] adds the contributions due to the finite wing tip vortices. One of the strengths of this model is the fact that these equations represent the only place where an empirical correlation is needed. Of course, this simplification comes with limitations, most notably the quasi-steady assumption—that the lift and drag forces are evaluated at each instant in time. Although this assumption holds better than one might deserve (e.g. [29,30,44]), and does ‘bundle in’ the effects of stable leading edge vortices [43,45], it cannot represent highly unsteady effects, most particularly shed vortices associated with, for example, rapid changes in the wing motion. This limitation will be discussed more in §4.1.

Previous reports of blade element models with application to animal flight (e.g. [30,44]) do not include wing camber. However, it is a particularly important morphological trait to include for accurate modelling of the membranous wings of bats, insects or birds with thin wings, and this feature is unique to the low order of model used here [29]. To assess the importance of camber, we performed two simulations using each set of flight kinematics. The first simulation modelled the wing including the full camber effect, while the second simulation modelled

each wing segment in the ‘traditional’ way—using the best-fit flat plate approximation to the measured wing geometry. The differences between the forces and power predicted using these two simulations will be discussed in §4.3 of Discussion.

## 2.2. Modelling the complete wing-body system and computing power

Fan & Breuer [29] showed that with this simulation framework they were able to predict the flight trajectory with good accuracy; however, contributions to flight power over a range of speeds have yet to be evaluated. Here, we extend the model to these estimates. To model the overall motion of the animal, we write the Lagrangian equation of motion of the three-point-mass system (body + two wings) in a global coordinate system  $\mathbf{G}$

$$\mathbf{D}(\mathbf{q})\ddot{\mathbf{q}} + \mathbf{C}(\mathbf{q}, \dot{\mathbf{q}})\dot{\mathbf{q}} + \mathbf{g}(\mathbf{q}) = \boldsymbol{\tau} + \mathbf{f}_{\text{aero}}, \quad (2.3)$$

where the generalized coordinate  $\mathbf{q}$  has 18 components (6 d.f. for the body, and  $2 \times 6$  d.f. for each wing).  $\mathbf{D}(\mathbf{q})$ ,  $\mathbf{C}(\mathbf{q}, \dot{\mathbf{q}})$  and  $\mathbf{g}(\mathbf{q})$  are the mass matrix, centrifugal matrix and gravitational vector respectively. The generalized torque,  $\boldsymbol{\tau} = [\boldsymbol{\tau}_b, \boldsymbol{\tau}_w]^T$  denotes the internal forces of the left and right wing with respect to the body, while  $\mathbf{f}_{\text{aero}} = [\mathbf{f}_{\text{ext}}, \mathbf{f}_w]^T$  represents the external aerodynamic forces and the ensuing torques felt by both left and right wing.

At each time  $t$ , since  $\mathbf{q}$  and its derivatives are known from the experimentally measured kinematics, the instantaneous total power  $P_{\text{tot}}$  is obtained as [10]

$$P_{\text{tot}}(t) = \boldsymbol{\tau}_w \dot{\mathbf{q}}_w, \quad (2.4)$$

where  $\dot{\mathbf{q}}_w$  are the generalized velocities for the two wings and  $\boldsymbol{\tau}_w$  are the generalized internal forces of the wing-body system. An equivalent expression, where power is computed as the product of applied torque and angular velocity, can be found in [31,46].

We assume that the effect of storage and release of elastic energy in muscles and tendons in the wing is small and can be neglected, although there is evidence that this phenomenon can occur in flying vertebrates [47,48]. A similar argument was made by Bahlman *et al.* [26] who used a robotic wing to emulate bat flight, and considered only the work done by the motor in estimating flight power. Thus, we calculate cycle-averaged power,  $\bar{P}_{\text{tot}}$ , from positive power only

$$\bar{P}_{\text{tot}} = 1/T \int_0^T P_{\text{tot}}^+ dt, \quad (2.5)$$

where  $P_{\text{tot}}^+ = [P_{\text{tot}}]^+$  ( $[\cdot]^+$  is an operator that only accepts non-negative values.)

To understand the relative importance of inertial and aerodynamic expenditure as a function of speed, we investigated



two hypothetical scenarios. In the first case, we calculate the power expended without aerodynamic forces. This translates to

$$\mathbf{f}_{\text{aero}} = \mathbf{0}, \quad (2.6)$$

in the Lagrangian equation of motion (equation (2.3)), which is equivalent to representing the wings as point masses that have no aerodynamic effect. In the second hypothetical case, we assume that the wing is massless—i.e. that there is no inertial power requirement. In all other respects, this case is identical to the full simulation, including all observed wing kinematics and deformations. This case zeros out the left side of equation (2.3), and thus the internal forces balance the entire aerodynamic forces and torques

$$\mathbf{0} = \boldsymbol{\tau} + \mathbf{f}_{\text{aero}}. \quad (2.7)$$

For each case, we calculate the power expenditure (equation (2.4)) resulting in the inertial power,  $P_{\text{inert}}$ , and the aerodynamic power,  $P_{\text{aero}}$ , respectively. The total power,  $P_{\text{tot}}$ , is not, however, simply the algebraic sum of the aerodynamic and inertial power, because there is an interaction between these forces, particularly during stroke reversal [9,33].

### 2.3. Decomposition of aerodynamic power

The aerodynamic power,  $P_{\text{aero}}$ , for a flying animal can also be broken down into the sum of the parasitic,  $P_{\text{par}}$ , induced,  $P_{\text{ind}}$ , and profile,  $P_{\text{pro}}$ , power [9]. If the animal is climbing, an additional climbing power term,  $P_{\text{clm}}$ , should be included to capture the associated rise in potential energy [17]

$$P_{\text{aero}} = P_{\text{par}} + P_{\text{ind}} + P_{\text{pro}} + P_{\text{clm}}. \quad (2.8)$$

The profile power,  $P_{\text{pro}}$ , characterizes the aerodynamic drag experienced by the wing, and is modelled as

$$P_{\text{pro}} = \mathbf{f}_{\text{ext}} \mathbf{u}, \quad (2.9)$$

where  $\mathbf{f}_{\text{ext}}$  is the sum of the aerodynamic forces experienced by each wing segment

$$\mathbf{f}_{\text{ext}} = \sum_i \mathbf{f}_i. \quad (2.10)$$

Here,  $i$  indexes the wing segment and  $\mathbf{u}$  is the instantaneous flight velocity. This is similar to the expression used in [21], except that  $\mathbf{f}_{\text{ext}}$  now also explicitly incorporates the effect of the flapping velocity seen by each segment [49].

The parasitic power,  $P_{\text{par}}$ , is associated with the components other than the wings—primarily the body—which we model as an additional segment

$$P_{\text{par}} = \mathbf{f}_{\text{body}} \mathbf{u}, \quad (2.11)$$

where the aerodynamic forces experienced by the body are estimated as

$$\mathbf{f}_{\text{body}} = -1/2\rho S_b C_d |\mathbf{u}|^2 \hat{\mathbf{i}} + 1/2\rho S_b C_l |\mathbf{u}|^2 \hat{\mathbf{k}}, \quad (2.12)$$

and  $S_b$  is the body planform area. The climbing power,  $P_{\text{clm}}$ , is modelled as

$$P_{\text{clm}} = -m\mathbf{g} \mathbf{u}, \quad (2.13)$$

where  $\mathbf{g}$  is the gravitational vector.

Finally, the induced power,  $P_{\text{ind}}$ , or power due to lift and thrust production, is associated with weight support [9], and ultimately comes from the downward momentum imparted by the two wings that support the animal's weight during flight. Since we have no way to directly compute this, it is obtained as the residual power, remaining after considering all other expenditures

$$P_{\text{ind}} = P_{\text{aero}} - P_{\text{pro}} - P_{\text{clm}} - P_{\text{par}}. \quad (2.14)$$

All of the contributions to power were cycle-averaged (equation (2.5)), and the mean value is used to measure the power expenditure at each flight speed.

### 2.4. Error estimation: Monte Carlo simulations

The measured kinematics and the quasi-steady lift and drag coefficients are subject to uncertainty, and we quantify the effects of these uncertainties using Monte Carlo simulations in which we repeat the simulation incorporating statistical variations of the input parameters into each calculation (as in [29]). Marker locations are assumed to have an uncertainty of 0.5 mm [34], and the wind tunnel speed has an uncertainty of  $\pm 0.2 \text{ m s}^{-1}$  [34]. All uncertainties are assumed to be uncorrelated. The constants in the equations for the lift and drag coefficients (equations (2.1) and (2.2)) were assigned a standard deviation (s.d.) of 2%. Each flight simulation was repeated 20 times, using kinematics and operating conditions that incorporated these uncertainties. Mean and s.d. of the flight powers were computed from this ensemble of simulations.

When comparing with published theoretical models [2,15], we employ a similar approach, assigning a generous uncertainty of 20% to morphological parameters such as the mass of the animal,  $m$ , body frontal area,  $S_b$ , and wing area,  $S$ .

## 3. Results

### 3.1. Flight kinematics

The majority of the flight kinematics for this dataset have been described earlier [34,37]. However, we report a few observations specifically relevant to the current discussion of modelling flight energetics.

Wing membrane camber changes considerably during the wingbeat cycle in both the arm- and handwing (figure 2a). The camber achieves its greatest magnitude during the upstroke (figure 2a, purple lines), and decreases monotonically with flight speed (figure 2b, purple symbols). The handwing camber has a lower maximum amplitude than that of the armwing, and is more consistent during the downstroke (figure 2a, gold lines). Unlike the armwing, the camber of the handwing is largely speed-independent (figure 2b, gold symbols).

The heavy bones of the armwing (humerus, forearm, femur, tibia and foot) dominate the mass distribution of the wing [37], and are closer to the wing root, and thus the trajectory of the centre of mass approximates a compact and localized ellipse in the  $y$ - $z$  plane of the body-centred coordinate system,  $\mathbf{B}$  (figure 3a). This elliptical shape remains stable across speeds (figure 3b), with the centre of ellipse located at approximately 1/4-span with a major axis radius approximately 10% of the maximum wingspan and oriented along  $z$ -axis of  $\mathbf{B}$ .

### 3.2. Aerodynamic force production versus flight speed

In figure 4a,b, we present weight support (vertical force in global coordinate system  $\mathbf{G}$ ) and thrust forces (or net horizontal forces, used interchangeably in this paper) associated with the handwing (gold), the armwing (purple) and the entire wing (green open circles), as a function of speed and normalized by the animal weight. For the low speed flights, the total weight support predicted is close to one, with the armwing contributing approximately 60% of weight support and the handwing providing the remaining 40%. At the highest

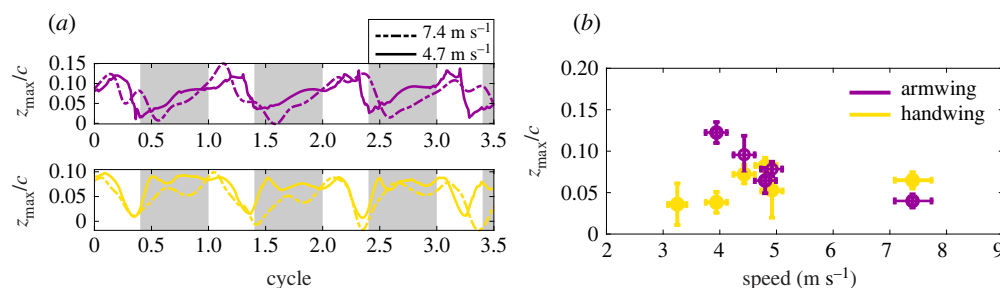


**Figure 2.** Wing camber in *Cynopterus brachyotis*. (a) Maximum camber,  $z_{\max}/c$ , for the armwing (1/4 span, purple) and handwing (3/4 span, gold). Shaded area indicates downstroke. (b) Camber,  $z/c$ , calculated at the phase of the wingbeat at which wingspan is maximum for either the armwing (purple) or the handwing (gold). The vertical bar indicates 1 s.d. of uncertainty based on Monte Carlo randomization, and the horizontal bar indicates 1 s.d. of wind tunnel speed.

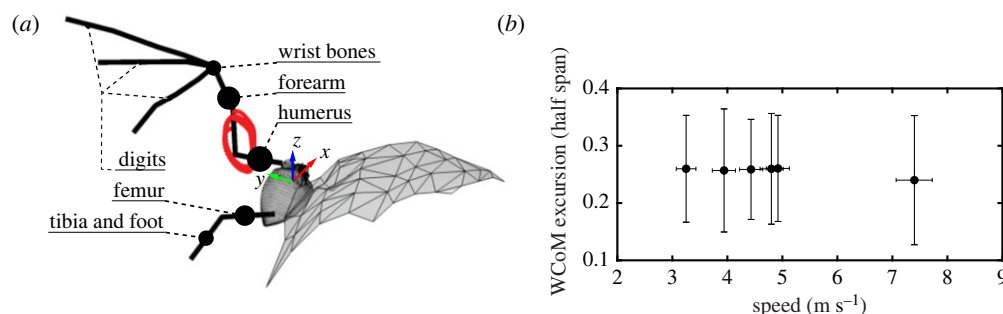


**Figure 3.** Wing centre of mass (WCoM). (a) Three-dimensional view of WCoM trajectories (red) in body-fixed coordinates, **B**. The relative weight of bones is indicated by size of black circles [37]. (b) The mean distance of the trajectories of WCoM as a function of flight speed. The vertical bars describe the maximum deviation from that mean distance, and the horizontal bar indicates 1 s.d. of wind tunnel speed. All quantities are normalized by the half span.

speed,  $U = 7.4 \text{ m s}^{-1}$ , the model exhibits 30% overprediction of the weight support force.

The cycle-averaged thrust/drag balance should be zero for a straight and steady flight, since thrust balances drag. However, the blade element momentum theory underpredicts total thrust for all speeds except at  $U = 7.4 \text{ m s}^{-1}$  (figure 4b). The armwing generates a negative  $x$ -force that remains relatively constant over all flight speeds, with a value of about 0.2–0.3 body weights. By contrast, the simulation indicates that the handwing has a neutral contribution to the thrust at low speeds, but generates positive thrust at  $U = 7.4 \text{ m s}^{-1}$ .

### 3.3. Power decomposition

The breakdown of flight power is summarized in table 1 as a function of flight speed. Note that positive sign of  $P_{\text{clm}}$  reflects the flight is climbing, whereas negative means it is in descending.

The total aerodynamic mass-specific power, expressed in  $\text{W kg}^{-1}$ , and its subcomponents—the parasitic, profile and induced power,  $P_{\text{ind}}$ ,  $P_{\text{pro}}$  and  $P_{\text{par}}$ —are shown in figure 5, along with comparisons drawn from published computational, experimental and theoretical studies. Overall, the results show good agreement. The total mass-specific power predicted using the model described here agrees well with published predictions of both Rayner's and Klein Heerenbrink's models (figure 5a) [2,15]. Note the climbing power is excluded from the total power, as the two theoretical models for straight and level flight do not include this term. Our predictions lie above the power estimates based on PIV measurements of Håkansson *et al.* [22,23] and von Busse *et al.* [21] (note those studies used bats that had a lower body mass than the *Cynopterus brachyotis* used in the

current study). Lastly, the computational study of *Hipposideros armiger*—a heavier (55 g) insectivorous bat [11]—predicted flight power closer to the Klein Heerenbrink's model, and is also greater than the predictions of our model.

The power breakdown of the parasitic, profile and induced powers (figure 5b–d) are also in good agreement with the theoretical models, both in absolute terms and in their speed trends (the PIV measurements did not allow the total power to be separated into the subcomponents).

Unique to the current approach, is the ability to tease apart the inertial and aerodynamic contributions to power, which are shown as a function of time in figure 6 for a moderate flight speed ( $U = 4.7 \text{ m s}^{-1}$ ). At each instant, the inertial power (red solid) reflects the inner product of generalized velocity,  $\dot{\mathbf{q}}_{\text{w}}$ , and the internal torque between wings and body,  $\boldsymbol{\tau}_{\text{w}}$  (equation 2.4).

If the negative values are also counted, the cycle-averaged inertial power (red line in figure 6) is close to zero ( $-0.008 \text{ [W]}$ ), reflecting that the aerodynamic forces are the only sources that dissipate energy, and that wing inertia and gravity are conservative forces.

The aerodynamic power,  $P_{\text{aero}}$  (blue line in figure 6), is positive during the majority of downstroke and into early upstroke, indicating power is supplied by the animal to overcome fluid forces; the power becomes negative during mid-upstroke, indicating that the fluid forces are assisting during this part of the wingbeat cycle. The net aerodynamic power is positive over the wingbeat cycle, because the wing kinematics are highly asymmetric during downstroke and upstroke. Overall, power is lost to the fluid due to viscous dissipation and vortex shedding into the wake.

The total power,  $P_{\text{tot}}$ , when both aerodynamic and inertial forces are included in the simulation (figure 6, black line), indicates that the peak power during the downstroke is assisted by

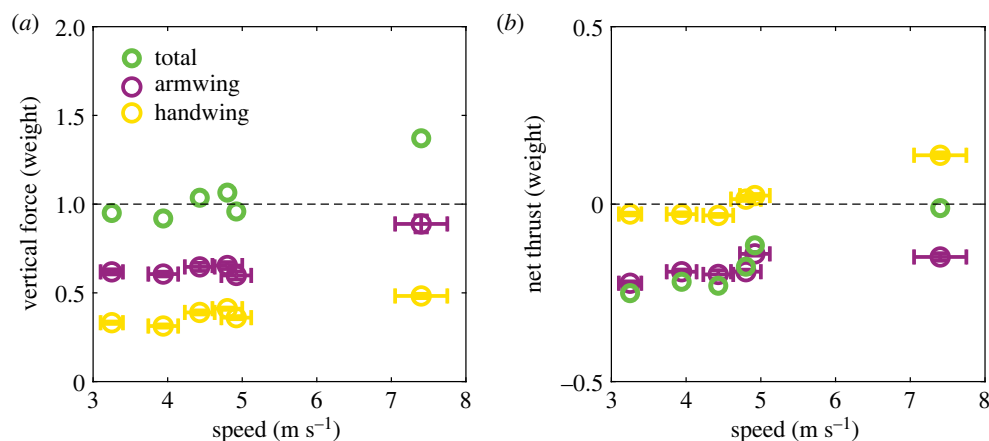


**Figure 4.** Cycle-averaged, weight-normalized (a) vertical force and (b) net thrust as a function of flight speed for handwing (gold), armwing (purple) and total (green open circles). The vertical bar indicates 1 s.d. of uncertainty resulting from the Monte Carlo randomization process, and the horizontal bar indicates 1 s.d. of wind tunnel speed.

**Table 1.** Power breakdown as a function of flight speed. Unless noted, all values are expressed as a percentage of the total power.

flight speed	$U$ (m s <sup>-1</sup> )	3.25	3.94	4.43	4.7	4.92	7.4
total power	$P_{\text{tot}}$ (W kg <sup>-1</sup> )	17.85	14.22	11.21	14.29	15.45	20.90
inertial	$P_{\text{inert}}/P_{\text{tot}}$ (%)	46.42	53.08	33.42	53.20	47.07	50.77
aerodynamic	$P_{\text{aero}}/P_{\text{tot}}$ (%)	82.48	76.85	96.47	79.91	94.58	94.30
profile	$P_{\text{pro}}/P_{\text{aero}}$ (%)	24.28	55.90	65.80	45.75	37.78	60.66
parasitic	$P_{\text{para}}/P_{\text{aero}}$ (%)	2.36	6.54	4.99	5.94	4.87	7.08
induced	$P_{\text{ind}}/P_{\text{aero}}$ (%)	17.80	16.18	25.85	13.66	37.59	17.26
climbing	$P_{\text{clm}}/P_{\text{aero}}$ (%)	38.05	-1.77	-0.16	14.55	14.35	9.30
effect of camber	$(P_{\text{tot}} - P_{\text{plate}})/P_{\text{tot}}$ (%)	8.50	8.16	15.60	24.01	14.01	24.94

the inertial power and thus is lower than the aerodynamic power requirement. Similarly, due to the contribution of inertial power, little power is required from the animal to raise the wing during the upstroke. Mid-downstroke is the only part of the wingbeat cycle in which inertial and aerodynamic forces combine, and in which the total power required is larger than either of the two individual components. When integrated over the wingbeat cycle, we find that the inertial power,  $P_{\text{inert}}$ , aerodynamic power,  $P_{\text{aero}}$ , and total power,  $P_{\text{tot}}$ , all vary with speed (figure 7), tracing a characteristic J shape with a local minimum around 4.3 m s<sup>-1</sup>.

A major feature of this study is the ability to assess the effect of wing camber on the prediction of the torque and power requirements for flight. This is shown as a function of time in figure 8a for the case of  $U = 4.3$  m s<sup>-1</sup>, and summarized over all flight speeds in figure 8b. The cycle-averaged mass-specific power when camber is included in the model is consistently higher than when the predicted power for a flat plate approximation of the observed kinematics is considered (figure 8b). This distinction is due to a significant difference between the flat plate and a cambered wing during the downstroke, when the power requirements are highest.

## 4. Discussion

The detailed spatial and temporal breakdown of the different contributions to the cost of flight that can identify force,

torque and power requirements associated with specific anatomical features of the animal (armwing, handwing, body etc.) at different phases during the wingbeat cycle (upstroke, downstroke) and over a range of flight speeds presented here advances our understanding of flight mechanics and energetics. Although high fidelity computational simulations [11,28,50] can, in principle, offer the same insight, they are prohibitively expensive and time-consuming. Wake-based studies using PIV data [7,8,21,22,25,51,52] can only access the ‘footprint’ of the aerodynamic cost of flight, while purely theoretical models [2,15] do not take advantage of the full wing and body kinematics and, although computationally attractive, offer only broad insights regarding to power requirements of flight. Here, we present a ‘Goldilocks’ solution—a model that enables a temporally and spatially detailed decomposition of key components of flight power, which is based on high-resolution kinematic measurements, and employs a tractable computational simulation. We provide power estimates with a level of detail that is typically provided only by CFD, but at a much lower computational cost; this opens avenues for modelling that have not previously been possible in a framework that is validated with results from animal flight recordings.

Although all of the flights analysed were steady and straight, there is always natural cycle-to-cycle variation in kinematics and in the subsequent forces, and there will be statistical uncertainty in the cycle-averaged quantities due to the low number of wing beats over which we can integrate. To assess the scale of this, we computed the s.d. of the vertical forces,  $F_z$ , computed for each wingbeat (a total of 16 cycles

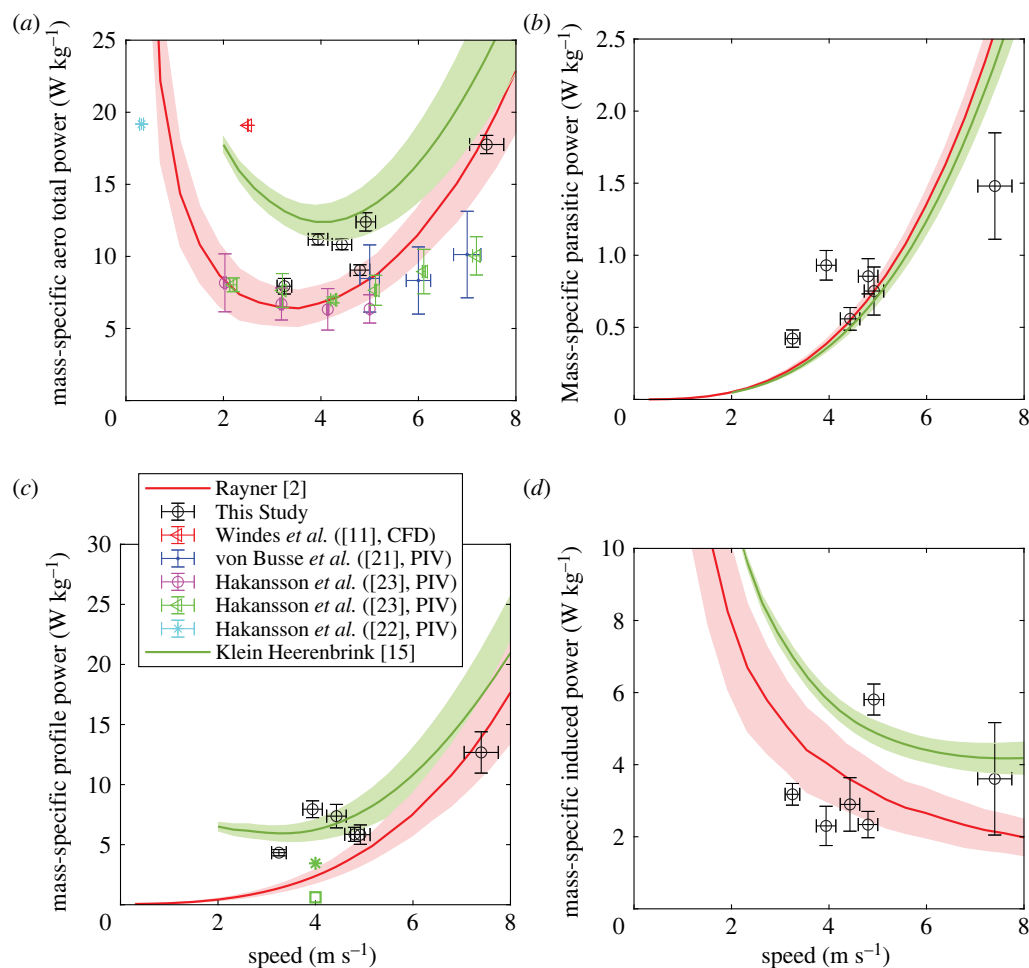


**Figure 5.** (a) Mass-specific aerodynamic power (climbing power excluded), and its breakdown into (b) parasitic, (c) profile and (d) induced power. In (c), at  $U = 4 \text{ m s}^{-1}$ , Klein Heerenbrink's original model for profile power (lift-dependent and zero-lift components included, green asterisk), and the model for just the zero-lift component (green square) are also presented. The vertical bar indicates 1 s.d. of uncertainty resulting from the Monte Carlo randomization process, and the horizontal bar indicates 1 s.d. of wind tunnel speed. Note Håkansson *et al.* [23] reports 95% CI instead of s.d.

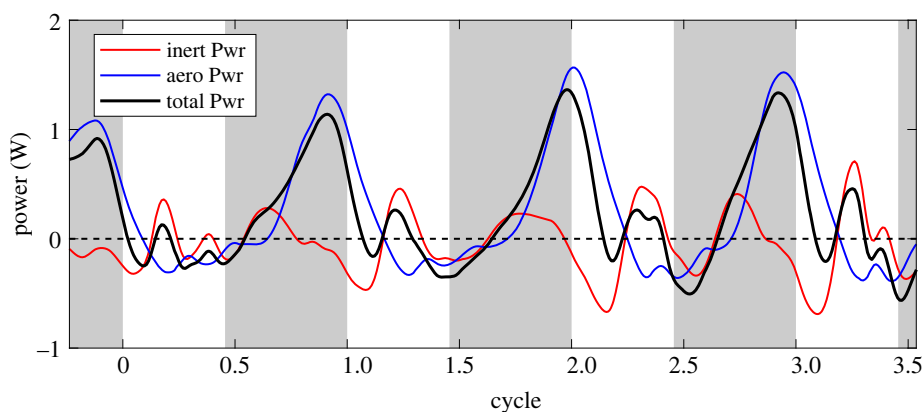


**Figure 6.** The power expenditure time series for inertial only (red), aerodynamic only (blue), and total power (black). The grey shading indicates downstroke. The flight speed is  $4.7 \text{ m s}^{-1}$ .

over all six flight speeds), finding that the s.d. was 0.096, or approximately 0.1 body weights. Although not negligible, this is reassuringly modest, and increases our confidence that the computed values and trends discussed are meaningful.

#### 4.1. Weight support, net force generation and model validation

To trust the insights provided by any computation, one must have faith in fidelity of the computational model. In straight

and level flight at constant speed, the predicted cycle-averaged vertical force should equal body weight, and thrust should equal drag (i.e. the net force in the flight direction should be zero). On this count, our quasi-steady model succeeds well, although there are some discrepancies. At low and medium flight speeds, the net vertical force closely approximates body weight (figure 4a); the balance between thrust and drag, while relatively constant, consistently underpredicts the net force by approximately 20% of body weight (figure 4b). Both vertical and horizontal force predictions rise at the highest flight speed measured. Consistent with



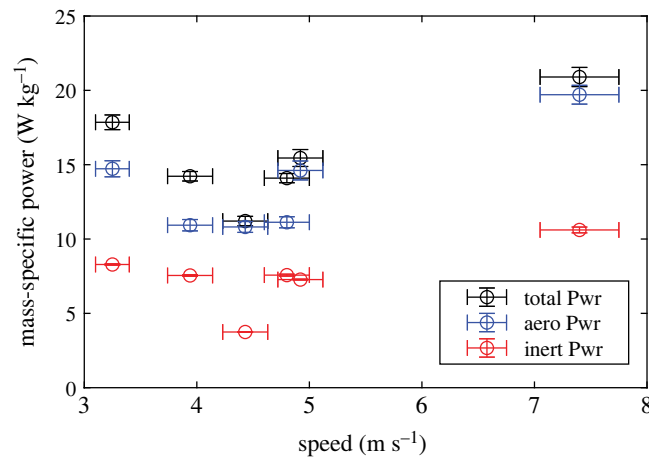


**Figure 7.** The variation of mass-specific aerodynamic (blue), inertial (red) and total mechanical power (black) with airspeed. Note for the inertial power (red), only positive values are counted towards the average. The vertical bar indicates the 1 s.d. of uncertainty resulting from Monte Carlo randomization process, and the horizontal bar indicates 1 s.d. of wind tunnel speed.

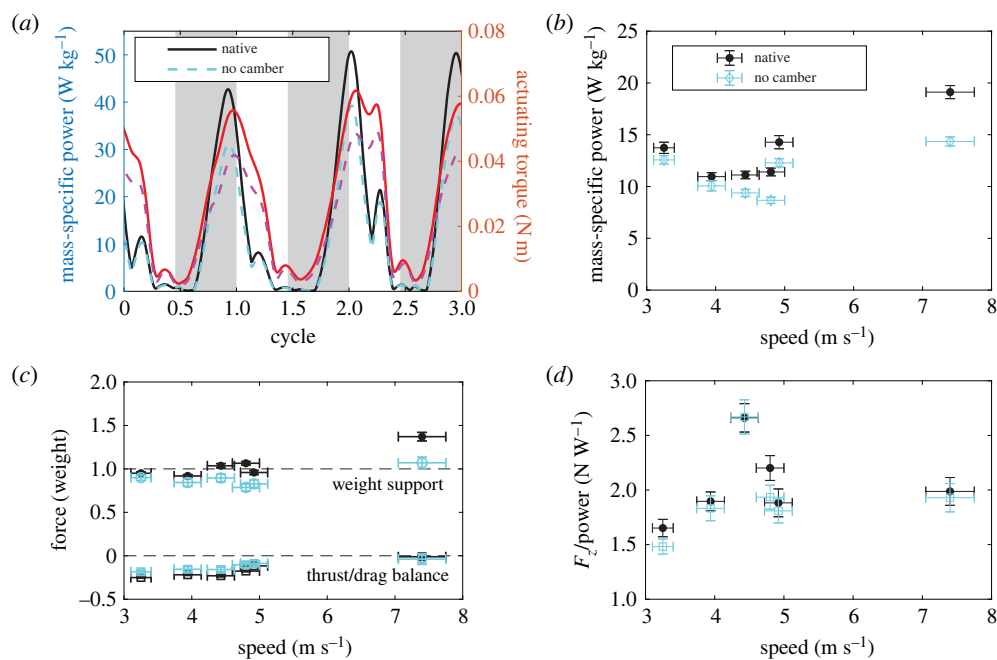


**Figure 8.** Effect of camber on actuating torque, aerodynamic power, force and power economy. In (a), at a medium flight speed of  $4.7 \text{ m s}^{-1}$ , the mass-specific power for native kinematics (solid black) is compared with the case without camber (dashed cyan). On the right axis, The torque output by the shoulder for native kinematics (solid red) is compared with the case without camber (dashed magenta). Grey shading indicates downstroke. In (b), typical aerodynamic power as a function of flight speed (black) is compared with the case without camber (cyan). In (c), cycle-averaged and weight-normalized vertical force  $F_z$  (circle) and thrust/drag balance (square) of native kinematics (black) are compared with the cases without camber (cyan) as a function of speed. In (d), power economy of native kinematics (black) and cases without camber (cyan) are compared for the ratio between vertical force  $F_z$  and aerodynamic power expenditure. For panels (b–d), the vertical bar indicates 1 s.d. of uncertainty resulting from a Monte Carlo randomization process, and the horizontal bar indicates 1 s.d. of wind tunnel speed.

the analysis of Shyy *et al.* [1], the armwing contributes more to the vertical force than the handwing, while the converse is true for forces in the flight direction. The armwing has a larger wetted surface area than the handwing, is more highly cambered and directs its net force more consistently in a vertically oriented direction. By contrast, the handwing, although it has a higher velocity and higher effective angle of attack (electronic supplementary material, figure S2), also experiences a negative angle of attack during upstroke due to wrist pronation [29].

The underprediction of net thrust is small (about 0.2 body weights), and might be explained by a number of effects. Since the net thrust force is the difference of two forces—one generated by the slight rotation of the net forces

associated with the wing motion, the other, the drag (viscous) forces—any small error in either the direction or amplitude of these two forces can have a relatively large effect on the net thrust. Secondly, with the exception of the wake model that accounts for the lift-induced drag associated with the tip vortex, our quasi-steady analysis does not account for the effects of other *unsteady* vortex systems generated during flight. Hedenstrom *et al.* [6] observed using PIV behind a nectar-feeding bat, *Glossophaga soricina*, at similar flight speeds, a thrust-producing vortex generated during the upstroke (see also Muijres *et al.* [52]), shed from the handwing due to a ‘backward flick’ motion [53]. Although the brief emergence of a negative angle of attack associated with the backward flip during upstroke is accounted for by the



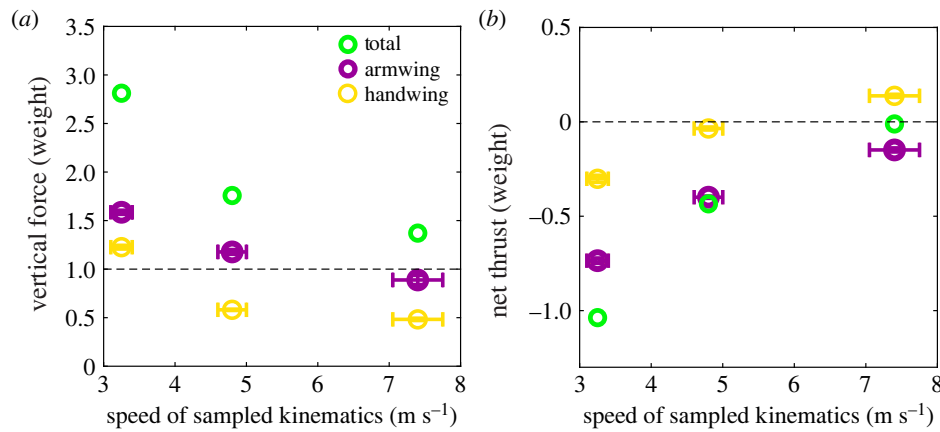


**Figure 9.** Simulations of flight using wing kinematics measured from slow ( $3.2 \text{ m s}^{-1}$ ), medium ( $4.7 \text{ m s}^{-1}$ ) and high speed flights ( $7.4 \text{ m s}^{-1}$ ) but *artificially enforcing a flight speed of  $7.4 \text{ m s}^{-1}$* . Sum of all the segment-wise aerodynamic forces for handwing (gold), armwing (purple) and total (green circles) are normalized by the body weight. The vertical bar indicates 1 s.d. of uncertainty resulting from a Monte Carlo randomization process, and the horizontal bar indicates 1 s.d. of wind tunnel speed.

BEMT [29], as mentioned earlier, shed vortices are not captured by the quasi-steady lift and drag model (equations (2.1) and (2.2)) and would result in a deficit in the prediction of net thrust. As flight speed increases, the effect of the backward flip decreases, and the prediction thus improves.

With respect to weight support, the surplus of vertical force at the highest speed (figure 4a) might also be attributed to the forming and shedding of an unsteady vortex that is not captured in the quasi-steady model. Muijres *et al.* [25] observed shedding of vortices from the handwing during upstroke at a high flight speed, and this ‘reversed vortex loop’, found only in bat flight [7,53], contributes to negative vertical force and positive thrust [51,53]. In addition, Hubel *et al.* [7] describe a vortex located at the wing–body junction early during the downstroke and present at all flight speeds (see also [6]). These root vortices represent a reduction in circulation close to the body, and thus less vertical force is generated. These root vortices may decrease in strength as the downstroke develops but persist throughout the cycle [25,54] (see also [7,8] for cases when they cease to exist and the wing–body behaves as a single wing with a relatively uniform circulation distribution). Since, in the current simulation, for simplicity, the body is represented as another flat lifting segment, this will result in an overprediction of the net vertical force during the beginning of the downstroke by the quasi-steady simulation. Furthermore, since the aerodynamic forces scale quadratically with speed, this overprediction of vertical force will be more pronounced at high than moderate flight speed (purple open circles in figure 4a).

In the context of this analysis, with the exception of the above scenarios during mid-upstroke and early downstroke, where unsteady vortex shedding might play a role, the majority of the aerodynamic forces are generated during downstroke [29], and for the range of flight speeds observed, the calculated effective angle of attack for both arm- and handwing near mid-downstroke are well below  $35^\circ$  (see electronic supplementary material, figure S2)—a critical value close to the stall angle for flapping-wing flight [55]. As a result, unsteady behaviour (forming and shedding) of the LEV [56] is probably not a dominating factor and thus the underlying aerodynamics can still be well-approximated by the quasi-steady assumption [29,30].

The wing kinematics differ substantially between the lowest ( $3.2 \text{ m s}^{-1}$ ) and highest ( $7.4 \text{ m s}^{-1}$ ) speeds studied, and these differences will have a substantial effect on the aerodynamic forces generated. We can use this to emphasize the accuracy of the quasi-steady aerodynamic calculation. To illustrate this, and to highlight the importance of using speed-dependent kinematics, we employ the wing kinematics measured at three different flight speeds,  $U = 3.2, 4.8$ , and  $7.4 \text{ m s}^{-1}$ , as the inputs for the calculations, *but enforce the bat’s forward flight speed of  $7.4 \text{ m s}^{-1}$* . The results of this thought experiment are shown in figure 9 and demonstrate that if a bat were to fly at  $7.4 \text{ m s}^{-1}$  using its demonstrated ‘low speed kinematics’ ( $3.2 \text{ m s}^{-1}$ ), its wings would generate vertical force equal to almost 300% body weight, and it would incur a net thrust deficit of 100% body weight. Using the intermediate speed kinematics observed at  $4.8 \text{ m s}^{-1}$  results in roughly 200% body weight in vertical force, and a thrust deficit of approximately 50%. Aerodynamic force production is, thus, highly sensitive to wing kinematics. At lower speeds, in which the dynamic pressure is lower, the wing motion needs to be tuned to generate higher lift coefficients, despite potential drag penalties. In this context, the discrepancy we observe between estimated vertical force and thrust (figure 4) are modest in comparison with the magnitude of change that relatively small modulations of flight kinematics can produce.

## 4.2. Power requirements for flight

The power predictions of the reduced-order model presented here compare well with predictions made using two leading theoretical models [2,15] (figure 5a).

The current results, and those of the analytical models, predict higher power than has been estimated from PIV wake measurements. However, the PIV results were obtained from smaller bat species (*Leptonycteris yerbabuenae*—approx. 26 g [22], *Plecotus auritus*, *Glossophaga soricina*—approx. 9 g [23] and *Carollia perspicillata*—approx. 15 g [21]); we note that mass-specific power is not necessarily independent of size [49].

The contribution to the parasitic power,  $P_{\text{par}}$ , is quite small (figure 5b and table 1), and our estimates show good agreement with the analytical models; all have a general

trend of power expenditure increasing with the cube of the flight speed.

Of the three primary components of total aerodynamic power  $P_{\text{aero}}$ —induced, parasitic and profile power—the profile power,  $P_{\text{pro}}$ , is particularly difficult to predict because the direction and strength of the airflow over the wing varies along the span [57]. Pennycuick's classic model [9], which assumes a constant value for  $P_{\text{pro}}$  over a wide range of speed, is generally considered to be too simplistic [21] and is not included here for comparison. However, the estimates of profile power from our calculations are similar to other models [2,15] ranging from 5 to 15 W kg<sup>-1</sup> over the speed range studied (figure 5c).

In Klein Heerenbrink's model [15], the profile drag is assumed to have both a lift-dependent and a zero-lift drag component. They assumed attached laminar flow, and employ a Blasius flat plate boundary layer solution to estimate the zero-lift drag [15]. However, local flow separation is likely to occur due to the high angles of attack [11], and the boundary layer may well be turbulent, as has been suggested by experiment [19]. To account for this, in our comparisons, we applied Klein Heerenbrink's model, but replaced the laminar boundary model for the zero-lift drag coefficient,  $C_{D0}$ , with a constant value of 0.085, which agrees well with the  $C_{D0}$  found in measurements on birds of similar size [20], and is also the zero-lift flat plate drag coefficient used in our blade element model (equation 2.2).

To quantitatively assess how the lift-dependent drag affects the profile power in Klein Heerenbrink's model, we calculated the profile power for the case of  $U = 4 \text{ m s}^{-1}$ , using the laminar boundary layer model for zero-lift drag estimation, but without lift-dependent drag (figure 5c, green square, 0.72 W kg<sup>-1</sup>). The original formula proposed by Klein Heerenbrink was also computed (figure 5c, green asterisk, 3.33 W kg<sup>-1</sup>) [15]. The difference between these two cases demonstrates the effect of lift-dependent profile power as it accounts for close to 80% of the profile power at this moderate flight speed. Furthermore, the difference between the original formula of Klein Heerenbrink (green asterisk) and the modified model (shaded green line in figure 5c) justifies the modification of the zero-lift drag coefficient,  $C_{D0}$ , which raises the minimum profile drag (figure 5c), improving the overall agreement between our calculations and the Klein Heerenbrink model.

In our quasi-steady reduced-order framework, the wake model produces an induced velocity field, or downwash [29], which has a larger impact on the effective angle of attack seen by each wing segment at moderate speeds than at higher flight speeds; this effect is similar to the lift-dependent model in Klein Heerenbrink *et al.* [15]. By contrast, Rayner's formulation does not include a lift-dependent component to the profile power estimation [2], and as mentioned, this is likely to be one of the reasons that Klein Heerenbrink's prediction agrees better with our low-order model than does the prediction using Rayner's model at slow/moderate speeds (3–5 m s<sup>-1</sup>). At higher speeds, the influence of the lift-dependent component in profile power,  $P_{\text{pro}}$ , diminishes and the profile power is dominated by the zero-lift drag; thus at these speeds our model fits well with both studies, and increases with the flight speed cubed, which quickly dominates the overall power expenditure.

In our approach, the induced power,  $P_{\text{ind}}$ , is not directly modelled but is defined as the power remaining after the parasitic power,  $P_{\text{par}}$ , the profile power,  $P_{\text{pro}}$ , and the climbing power,  $P_{\text{clm}}$ , are subtracted from the full aerodynamic power (equation 2.14). A similar treatment was made with profile power in [23]. By contrast, previous work has assumed an empirical induced power factor ( $\kappa$  in [9]), which has been controversial [15], ranging from a low of 0.9 [58] to 1.8 [15], or even 2.5 [23]. Our predictions cluster closely around the two theoretical predictions: Rayner used a  $\kappa$  of 1.2 [2,21], and Klein Heerenbrink's  $\kappa$  is a variable derived from an optimization scheme, which varies with freestream flapping frequency [15].

Some studies suggest that the capacity of tendons to store and release elastic strain energy could influence whole body energetics of flying animals, as it does in terrestrial locomotion [9,47,48]. However, we do not include this effect, and as a result average total power is not the simple algebraic sum of the aerodynamic power and inertial power; this has been pointed out by previous studies [9,33]. Specifically, the aerodynamic power is greater than the total power towards the end of downstroke (figure 6). This finding may seem counterintuitive, but arises as a consequence of balancing relatively high wing inertia and aerodynamic loading, which leads to a reduced requirement for force to actuate wing motion (figure 6, black line) compared with the case without inertial effects (figure 6, blue line). Analysis of inertial and aerodynamic forces in cockatiel flight also led to the suggestion that wing inertial effects alleviated the total cost of flight [44]. We predict that almost no additional power is needed to move the wing during the upstroke (black line) because the aerodynamic forces alone are sufficient to overcome wing mass.

The average inertial power stays relatively constant—around 8 W kg<sup>-1</sup>—with respect to speed, and is always smaller than the aerodynamic power (figure 7). The consistency of the inertial power is due to the fact that the wing centre of mass trajectory shows no speed-dependence (figure 3b) and the flapping frequency is relatively constant near 10 Hz (see electronic supplementary material, figure S1; also see [34]). These values are slightly higher than those estimated by Norberg [32], who studied the flight of the brown long-eared bat, *Plecotus auritus*, body mass approximately 9 g, during slow flight at approximately 2.4 m s<sup>-1</sup>. In that case, the inertial power was around 7 W kg<sup>-1</sup>. Later, Norberg *et al.* [18] estimated the inertial power of a nectar-feeding bat, *Glossophaga soricina*, (body mass approx. 10 g) to be 6 W kg<sup>-1</sup> at a flight speed of 4.2 m s<sup>-1</sup>, and as high as 25 W kg<sup>-1</sup> during hovering. Neither Rayner [14] nor Pennycuick [9] included inertial power as part of the cost of flight in their models. Rayner deemed inertial power negligible, while Pennycuick argued that the 'wing's kinetic energy is a high-grade form of energy', and would be reconverted to aerodynamic power.

Much like the variation of kinetic energy for a swinging pendulum, the kinetic energy of the wing modulates over a period of approximately  $T/2$  (figure 6), where  $T$  is the flapping period. Although the kinematics of the handwing vary more significantly with speed (electronic supplementary material, figure S2), the very low mass of this part of the wing leads to a negligible effect on the inertial power requirements. In all, motion of the heavy armwing is relatively invariant to speed changes, and the necessary adjustment associated with aerodynamics is made using the light handwing.

### 4.3. The role of camber

Camber decreases with increasing speed in the armwing, which was also reported by Riskin *et al.* [38] for several bat species, including *Cynopterus brachyotis* (the same dataset as we use here). Riskin *et al.*, however, only reported on the general trend of camber versus flight speed, while here we add more details, including the comparison between camber in the armwing and handwing, the time dependence of the wing camber in both the proximal and distal portions of the wing, and lastly, the impact of camber on energetics. Von Busse *et al.* observed a strikingly similar trend of decrease in chord-normalized camber from 0.14 to 0.04 as flight speed increased from hovering to  $7 \text{ m s}^{-1}$  in the 21 g nectar feeding bat, *Leptonycteris yerbabuenae* [35].

In straight, level, non-accelerating flight, vertical force remains equal to weight regardless of speed. Wing area does not change substantially in downstroke [34] when flight speed and dynamic pressure,  $\rho U^2$ , increase, hence the lift coefficient of the wing must decrease (equation 2.1). Reducing the effective angle of attack ( $\alpha$ , see electronic supplementary material, figure S2) and reducing the wing camber ( $z_{\text{max}}/c$ , figure 2b) are both mechanisms used to effect such a change (see also [38]).

Bats have the potential to actively modulate the mechanical compliance of the wing membrane in the armwing using the *plagiopatagiales proprii*—muscles that are embedded in the skin of the armwing and are known to be more active during downstroke than upstroke [36]. The activation of these muscles modulates camber of the highly elastic skin membrane [59]. Cheney *et al.*'s results [36] show increased muscle activity at higher flight speeds, suggesting that they are used to achieve what we observe here—a marked reduction in armwing camber as flight speed increases (figure 2b).

In our simulations, the predicted vertical force when camber is not included is always smaller than that of the native kinematics and, at low/medium flight speeds, is not sufficient to support the animal's body weight (figure 8c). By contrast, the forces estimated while including the effect of wing camber satisfy weight support, but are accompanied by a slightly higher power requirement, especially at mid- and late downstroke (figure 8a) for all flight speeds (figure 8b). On the other hand, the net thrust increases slightly with the inclusion of camber. In addition, the 'power economy' [4,5]—the ratio between weight support ( $F_z$  in global coordinate system  $\mathbf{G}$ ) and the corresponding power (figure 8d)—is higher for native kinematics than for cases excluding the effect of camber, suggesting that camber boosts lift on a per-watt basis. CFD modelling of the desert locust, *Schistocerca gregaria* [4], and a painted lady butterfly, *Vanessa cardui* [5], show similar results.

### 4.4. Bat-inspired guidelines for robotic flapping wing design

Three important messages may be drawn from this study of arm/handwing kinematics as a function of speed, and used to inform the design of flapping wing robots. First, in this study, bat wing mass distribution is concentrated close to the wing's centre of rotation, far from the wingtip, to minimize a large inertial power penalty [60], and this anatomical structure should be implemented in flapping devices. Second, in bats, flapping frequency and wingbeat amplitude change little with flight speed, but camber

declines significantly, and demonstrates an important influence on the flight energetics. Nevertheless, we see that camber does improve the force per watt (figure 8d), and suggests that active camber control adapted to flight speed is important and might be implemented in robotic systems using, for example, dielectric elastomers [61,62]. Third, the distal handwing kinematics are more sensitive to flight speed than those of the proximal armwing. This strategy calls to mind the proximo-distal gradient in joint neuromechanical control found in fast-running guinea fowl, *Numida meleagris* [63], where the proximal muscles are controlled in a feed-forward manner and exhibit load-insensitive mechanical performance, while the distal muscle output is highly load-sensitive. In the bat subjects of this study, pitch angle varies along the wing span (i.e. the wing twists), reducing effective angle of attack in the handwing, and serving to reorient the resultant aerodynamic force in a manner that increases thrust (figure 4b). Simulation of bat-like robots has recently shown [64] that wing twist synergistically combined with wing folding can reduce negative lift during upstroke and convert the effective angle of attack from negative to positive. In doing so, one can reduce the overall cost of flight. Similarly, the adoption of wing twist and speed-dependent changes in pitch angle have been shown analytically to produce beneficial aerodynamic results in bird flight [33].

## 5. Conclusion

In this paper, we used a reduced-order model [29], and demonstrated the distinct roles of the arm- and handwing for force production. For moderate flight speeds, the arm- and handwing consistently contribute around 60% and 40%, respectively, to the vertical force, whereas the handwing consistently generates more thrust than the armwing (figure 4). In addition, the power prediction from our model aligns well with existing CFD, experimental, and theoretical predictions for straight and level flight data. Every flight model has its strengths and weaknesses, some requiring extensive computational effort, others providing useful predictions, albeit with low temporal or spatial resolution, but at very low computational cost. Although our model requires quasi-steady aerodynamic coefficients, it otherwise avoids using empirical coefficients, and achieves detailed force predictions, and at a much cheaper cost than CFD.

Moreover, inertial power, which is predominantly associated with the motion of the heavier armwing, is relatively insensitive to flight speed, and centres around  $8 \text{ W kg}^{-1}$  as flapping frequency changes little with speed (electronic supplementary material, figure S1a, and figure 3b). On the other hand, the aerodynamic power is much more sensitive to speed, and varies from 12 to  $20 \text{ W kg}^{-1}$ , with the minimum centred around  $U = 4.3 \text{ m s}^{-1}$  (figure 7). In our model, we demonstrate the subtle interaction between aerodynamic and inertial forces: part of the momentum of the massed wing is used by the shoulder to balance the aerodynamic force, and the aerodynamic force, in turn, acts to assist in elevating the wing early in the upstroke. As a result, less power is required, especially during stroke reversal (figure 6).

A major feature of the model is the assessment of the role of wing camber in force and power requirements. The maximum chord-normalized armwing camber decreases from 0.15 to 0.05 as flight speed increases, whereas handwing camber demonstrates no clear trend (figure 2b). Even though power



requirements increase when the wing camber is included in the simulation—rising from 8% to 25% as flight speed increases from 3.2 to 7.4 m s<sup>-1</sup>—the camber also contributes to a significant increase in the cycle-averaged vertical force.

Finally, we recommend that robotic design would benefit from (i) locating most of the wing mass close to the wing root, so as to minimize the penalty on moment of inertia and (ii) employing a load-insensitive, steady flapping motion at the shoulder, coupled with a variable camber armwing and/or adjustable kinematics in the distal ‘handwing’, in order to affect flight-speed dependent force generation.

**Data accessibility.** Our model used experimental data recorded by Riskin *et al.* [34], and is curated and preprocessed to suit this study. We have uploaded these data as electronic supplementary material [65].

## References

- Shyy W, Aono H, Kang C-K, Liu H. 2013 *An introduction to flapping wing aerodynamics*. Cambridge, UK: Cambridge University Press.
- Rayner JMV. 1979 A new approach to animal flight mechanics. *J. Exp. Biol.* **80**, 17–54. (doi:10.1242/jeb.80.1.17)
- Dickinson MH, Lehmann FO, Sane SP. 1999 Wing rotation and the aerodynamic basis of insect flight. *Science* **284**, 1954–1960. (doi:10.1126/science.284.5422.1954)
- Young J, Walker SM, Bomphrey RJ, Taylor GK, Thomas ALR. 2009 Details of insect wing design and deformation enhance aerodynamic function and flight efficiency. *Science* **325**, 1549–1552. (doi:10.1126/science.1175928)
- Zheng L, Hedrick TL, Mittal R. 2013 Time-varying wing-twist improves aerodynamic efficiency of forward flight in butterflies. *PLoS ONE* **8**, 1–10. (doi:10.1371/journal.pone.0053060)
- Hedenström A, Johansson LC, Wolf M, Von Busse R, Winter Y, Spedding GR. 2007 Bat flight generates complex aerodynamic tracks. *Science* **316**, 894–897. (doi:10.1126/science.1142281)
- Hubel TY, Riskin DK, Swartz SM, Breuer KS. 2010 Wake structure and wing kinematics: the flight of the lesser dog-faced fruit bat, *Cynopterus brachyotis*. *J. Exp. Biol.* **213**, 3427–3440. (doi:10.1242/jeb.043257)
- Hubel TY, Hristov NI, Swartz SM, Breuer KS. 2016 Wake structure and kinematics in two insectivorous bats. *Phil. Trans. R. Soc. B* **371**, 20150385. (doi:10.1098/rstb.2015.0385)
- Pennycuik CJ. 2008 *Modelling the flying bird*. New York, NY: Academic Press.
- Parslew B. 2015 Predicting power-optimal kinematics of avian wings. *J. R. Soc. Interface* **12**, 20140953. (doi:10.1098/rsif.2014.0953)
- Windes P, Fan X, Bender M, Tafti DK, Müller R. 2018 A computational investigation of lift generation and power expenditure of Pratt’s roundleaf bat (*Hipposideros pratti*) in forward flight. *PLoS ONE* **13**, e0207613. (doi:10.1371/journal.pone.0207613)
- Leishman JG. 2006 *Principles of helicopter aerodynamics*. Cambridge, UK: Cambridge University Press.
- Rayner JMV. 1979 A vortex theory of animal flight. Part 1. The vortex wake of a hovering animal. *J. Fluid Mech.* **91**, 697–730. (doi:10.1017/s0022112079000410)
- Rayner JMV. 1979 A vortex theory of animal flight. Part 2. The forward flight of birds. *J. Fluid Mech.* **91**, 731–763. (doi:10.1017/s0022112079000422)
- Heerenbrink MK, Johansson LC, Hedenström A. 2015 Power of the wingbeat: modelling the effects of flapping wings in vertebrate flight. *Proc. R. Soc. A* **471**, 20140952. (doi:10.1098/rspa.2014.0952)
- Hedrick TL, Tobalske BW, Biewener AA. 2003 How cockatiels (*Nymphicus hollandicus*) modulate pectoralis power output across flight speeds. *J. Exp. Biol.* **206**, 1363–1378. (doi:10.1242/jeb.00272)
- MacAyeal LC, Riskin DK, Swartz SM, Breuer KS. 2011 Climbing flight performance and load carrying in lesser dog-faced fruit bats (*Cynopterus brachyotis*). *J. Exp. Biol.* **214**, 786–793. (doi:10.1242/jeb.050195)
- Norberg UM, Kunz TH, Steffensen JF, Winter Y, von Helversen O. 1993 The cost of hovering and forward flight in a nectar-feeding bat, *Glossophaga soricina*, estimated from aerodynamic theory. *J. Exp. Biol.* **182**, 207–227. (doi:10.1242/jeb.182.1.207)
- Murphy JT, Hu H. 2010 An experimental study of a bio-inspired corrugated airfoil for micro air vehicle applications. *Exp. Fluids* **49**, 531–546. (doi:10.1007/s00348-010-0826-z)
- Withers PC. 1981 An aerodynamic analysis of bird wings as fixed aerofoils. *J. Exp. Biol.* **90**, 143–162. (doi:10.1242/jeb.90.1.143)
- von Busse R, Waldman RM, Swartz SM, Voigt CC, Breuer KS. 2014 The aerodynamic cost of flight in the short-tailed fruit bat (*Carollia perspicillata*): comparing theory with measurement. *J. R. Soc. Interface* **11**, 20140147. (doi:10.1098/rsif.2014.0147)
- Håkansson J, Hedenström A, Winter Y, Johansson LC. 2015 The wake of hovering flight in bats. *J. R. Soc. Interface* **12**, 20150357. (doi:10.1098/rsif.2015.0357)
- Håkansson J, Jakobsen L, Hedenström A, Johansson LC. 2017 Body lift, drag and power are relatively higher in large-eared than in small-eared bat species. *J. R. Soc. Interface* **14**, 20170455. (doi:10.1098/rsif.2017.0455)
- Johansson LC, Jakobsen L, Hedenström A. 2018 Flight in ground effect dramatically reduces aerodynamic costs in bats. *Curr. Biol.* **28**, 3502–3507. (doi:10.1016/j.cub.2018.09.011)
- Muijres FT, Johansson LC, Winter Y, Hedenström A. 2011 Comparative aerodynamic performance of flapping flight in two bat species using time-resolved wake visualization. *J. R. Soc. Interface* **8**, 1418–1428. (doi:10.1098/rsif.2011.0015)
- Bahlman JW, Swartz SM, Breuer KS. 2013 Design and characterization of a multi-articulated robotic bat wing. *Bioinspir. Biomim.* **8**, 16009. (doi:10.1088/1748-3182/8/1/016009)
- Bahlman JW, Swartz SM, Breuer KS. 2014 How wing kinematics affect power requirements and aerodynamic force production in a robotic bat wing. *Bioinspir. Biomim.* **9**, 25008. (doi:10.1088/1748-3182/9/2/025008)
- Sekhar S, Windes P, Fan X, Tafti DK. 2018 Canonical description of wing kinematics and dynamics for a straight flying insectivorous bat *Hipposideros pratti*. *PLoS ONE* **14**, e0218672. (doi:10.1371/journal.pone.0218672)
- Fan X, Breuer K. 2022 Low-order modeling of flapping flight with highly articulated, cambered, heavy wings. *AIAA J.* **60**, 892–901. (doi:10.2514/1.j.606661)
- Song J, Luo H, Hedrick TL. 2015 Performance of a quasi-steady model for hovering hummingbirds. *Theor. Appl. Mech. Lett.* **5**, 50–53. (doi:10.1016/j.taml.2014.12.003)
- Vejdani HR, Boerma DB, Swartz SM, Breuer KS. 2018 The dynamics of hovering flight in hummingbirds, insects and bats with implications for aerial robotics. *Bioinspir. Biomim.* **14**, 016003. (doi:10.1088/1748-3190/aaba56)



32. Norberg UM. 1976 Aerodynamics, kinematics, and energetics of horizontal flapping flight in the long-eared bat *Plecotus auritus*. *J. Exp. Biol.* **65**, 179–212. (doi:10.1242/jeb.65.1.179)
33. Parslew B. 2012 Simulating avian wingbeats and wakes. PhD thesis, University of Manchester, UK.
34. Riskin DK, Willis DJ, Iriarte-Diaz J, Hedrick TL, Kostandov M, Chen J, Laidlaw DH, Breuer KS, Swartz SM. 2008 Quantifying the complexity of bat wing kinematics. *J. Theor. Biol.* **254**, 604–615. (doi:10.1016/j.jtbi.2008.06.011)
35. Von Busse R, Hedenström A, Winter Y, Johansson LC, Hedenstrom A, Winter Y, Johansson LC. 2012 Kinematics and wing shape across flight speed in the bat, *Leptonycteris yerbabuenae*. *Biol. Open* **1**, 1226–1238. (doi:10.1242/bio.20122964)
36. Cheney JA, Konow N, Middleton KM, Breuer KS, Roberts TJ, Glibin EL, Swartz SM. 2014 Membrane muscle function in the compliant wings of bats. *Bioinspir. Biomim.* **9**, 025007. (doi:10.1088/1748-3182/9/2/025007)
37. Riskin DK, Bergou A, Breuer KS, Swartz SM. 2012 Upstroke wing flexion and the inertial cost of bat flight. *Proc. R. Soc. B* **279**, 2945–2950. (doi:10.1098/rspb.2012.0346)
38. Riskin DK, Iriarte-Diaz J, Middleton KM, Breuer KS, Swartz SM. 2010 The effect of body size on the wing movements of pteropodid bats, with insights into thrust and lift production. *J. Exp. Biol.* **213**, 4110–4122. (doi:10.1242/jeb.043091)
39. Taylor GK, Nudds RL, Thomas AL. 2003 Flying and swimming animals cruise at a Strouhal number tuned for high power efficiency. *Nature* **425**, 707–711. (doi:10.1038/nature02000)
40. Anderson JD. 2010 *Fundamentals of aerodynamics*. New York, NY: McGraw-Hill Education.
41. Riskin DK, Bahlman JW, Hubel TY, Ratcliffe JM, Kunz TH, Swartz SM. 2009 Bats go head-under-heels: the biomechanics of landing on a ceiling. *J. Exp. Biol.* **212**, 945–953. (doi:10.1242/jeb.026161)
42. Glauert H. 1983 *The elements of aerofoil and airscrew theory*. Cambridge, UK: Cambridge University Press.
43. Usherwood JR. 2009 The aerodynamic forces and pressure distribution of a revolving pigeon wing. *Exp. Fluids* **46**, 991–1003. (doi:10.1007/s00348-008-0596-z)
44. Hedrick TL, Usherwood JR, Biewener AA. 2004 Wing inertia and whole-body acceleration: an analysis of instantaneous aerodynamic force production in cockatiels (*Nymphicus hollandicus*) flying across a range of speeds. *J. Exp. Biol.* **207**, 1689–1702. (doi:10.1242/jeb.00933)
45. Muijres FT, Johansson LC, Barfield R, Wolf M, Spedding GR, Hedenström A. 2008 Leading-edge vortex improves lift in slow-flying bats. *Science* **319**, 1250–1253. (doi:10.1126/science.1153019)
46. Berman GJ, Wang ZJ. 2007 Energy-minimizing kinematics in hovering insect flight. *J. Fluid Mech.* **582**, 153–168. (doi:10.1017/s0022112007006209)
47. Biewener AA, Corning WR, Tobalske BW. 1998 In vivo pectoralis muscle force-length behavior during level flight in pigeons (*Columba livia*). *J. Exp. Biol.* **201**, 3293–3307. (doi:10.1242/jeb.201.24.3293)
48. Konow N, Cheney JA, Roberts TJ, Waldman JRS, Swartz SM. 2015 Spring or string: does tendon elastic action influence wing muscle mechanics in bat flight? *Proc. R. Soc. B* **282**, 1–7. (doi:10.1098/rspb.2015.1832)
49. Norberg UM. 1990 *Vertebrate flight: mechanics, physiology, morphology, ecology and evolution*, vol. 27. Berlin, Germany: Springer Science & Business Media.
50. Fan X, Windes P, Tafti D, Sekhar S, Bender M, Kurdila A, Mueller R. 2018 Proper orthogonal decomposition of straight and level flight kinematics in an insectivorous bat. In *2018 AIAA Modeling and Simulation Technologies Conf.*, number 209959. Reston, Virginia: American Institute of Aeronautics and Astronautics. (doi:10.2514/6.2018-2155).
51. Muijres FT, Spedding GR, Winter Y, Hedenström A. 2011 Actuator disk model and span efficiency of flapping flight in bats based on time-resolved PIV measurements. *Exp. Fluids* **51**, 511–525. (doi:10.1007/s00348-011-1067-5)
52. Muijres FT *et al.* 2014 Leading edge vortices in lesser long-nosed bats occurring at slow but not fast flight speeds. *Bioinspir. Biomim.* **9**, 025006. (doi:10.1088/1748-3182/9/2/025006)
53. Hedenström A, Johansson LC. 2015 Bat flight: aerodynamics, kinematics and flight morphology. *J. Exp. Biol.* **218**, 653–663. (doi:10.1242/jeb.031203)
54. Muijres FT, Johansson LC, Bowlin MS, Winter Y, Hedenström A. 2012 Comparing aerodynamic efficiency in birds and bats suggests better flight performance in birds. *PLoS ONE* **7**, e37335. (doi:10.1371/journal.pone.0037335)
55. Wang ZJ, Birch JM, Dickinson MH. 2004 Unsteady forces and flows in low Reynolds number hovering flight: two-dimensional computations vs robotic wing experiments. *J. Exp. Biol.* **207**, 449–460. (doi:10.1242/jeb.00739)
56. Taha HE, Hajj MR, Beran PS. 2014 State-space representation of the unsteady aerodynamics of flapping flight. *Aerosp. Sci. Technol.* **34**, 1–11. (doi:10.1016/j.ast.2014.01.011)
57. Pennycuik CJ. 1968 Power requirements for horizontal flight in the pigeon *Columba livia*. *J. Exp. Biol.* **49**, 527–555. (doi:10.1242/jeb.49.3.527)
58. Pennycuik CJ, Åkesson S, Hedenström A. 2013 Air speeds of migrating birds observed by ornithodolite and compared with predictions from flight theory. *J. R. Soc. Interface* **10**, 20130419. (doi:10.1098/rsif.2013.0419)
59. Cheney JA, Rehm JC, Swartz SM, Breuer KS. 2022 Bats actively modulate membrane compliance to control camber and reduce drag. *J. Exp. Biol.* **225**, jeb243974. (doi:10.1242/jeb.243974)
60. Send W, Fischer M, Jebens K, Mugrauer R, Nagarathinam A, Scharstein F. 2012 Artificial hinged-wing bird with active torsion and partially linear kinematics. In *28th Congress of the Int. Council of the Aeronautical Sciences (ICAS)*, pp. 23–28. Edinburgh, UK: International Council of the Aeronautical Sciences.
61. Curet OM, Carrere A, Waldman R, Breuer KS. 2014 Aerodynamic characterization of a wing membrane with variable compliance. *AIAA J.* **52**, 1749–1756. (doi:10.2514/1.j052688)
62. Bohnker JR, Breuer KS. 2019 Control of separated flow using actuated compliant membrane wings. *AIAA J.* **57**, 3801–3811. (doi:10.2514/1.j058277)
63. Daley MA, Felix G, Biewener AA. 2007 Running stability is enhanced by a proximo-distal gradient in joint neuromechanical control. *J. Exp. Biol.* **210**, 383–394. (doi:10.1242/jeb.02668)
64. Fan X, Breuer K, Vejdani H. 2021 Wing fold and twist greatly improves flight efficiency for bat-scale flapping wing robots. In *2021 IEEE Int. Conf. Intell. Robots Syst. (IROS), Piscataway, NJ*, pp. 7391–7397. (doi:10.1109/iros51168.2021.9636735)
65. Fan X, Swartz S, Breuer K. 2022 Power requirements for bat-inspired flapping flight with heavy, highly articulated and cambered wings. Figshare. (doi:10.6084/m9.figshare.c.6181102)